Inorganic Chemistry

Article

pubs.acs.org/IC

Phase-Dependent Enhancement of the Green-Emitting Upconversion Fluorescence in $LaVO_4$:Yb^{3+}, Er^{3+}

Feng Zhang,*[†,‡] Guoqiang Li,[†,‡] Weifeng Zhang,[†,‡] and Yu Li Yan*[†]

[†]School of Physics and Electronics, Henan University, Kaifeng 475004, People's Republic of China

[‡]Key Lab of Photovoltaic Materials of Henan Province, Kaifeng 475001, People's Republic of China

ABSTRACT: The phase-dependent upconversion luminescence properties of $LaVO_4$:Er^{3+} were studied to provide new insights into the design of new upconversion materials with high efficiency. Er^{3+}-, Yb^{3+}/Er^{3+}-doped t-$LaVO_4$ microcrystals were successfully synthesized by the disodium ethylenediaminetetraacetic acid (Na_2EDTA)-assisted hydrothermal method. X-ray diffraction (XRD), inductively coupled plasma optical emission spectrometer (ICP-OES), Fourier transform infrared spectroscopy (FT-IR), scanning electron microscopy (SEM), transmission electron microscopy (TEM), Raman spectroscopy, luminescence spectroscopy, and thermogravimetric analysis (TGA) were used to characterize the samples. The results indicated that t-$LaVO_4$ presents sheaf-like morphology, and the possible formation mechanism for these sheaves was proposed on the basis of time-dependent experiments. Furthermore, the phase-dependence (i.e., monoclinic- and tetragonal-type) upconversion luminescence properties were systematically studied, and the upconversion mechanisms were proposed according to spectral, pump power, and the concentration of Yb^{3+} dependence analyses. It is worthwhile pointing out that the Er^{3+}-doped t-$LaVO_4$ exhibits a brighter green emission, which is approximately 10 times that of m-$LaVO_4$:Er^{3+} using a continuous 980 nm laser diode as the excitation source. This remarkable improvement was rationally analyzed on the basis of the composition, crystal structures, Raman spectra, morphology, and size. The comparative experiments suggest that the local structure of Er^{3+} was considered as an important reason for the higher fluorescence intensity of t-$LaVO_4$:Er^{3+}, which was also confirmed by the results of density functional theory (DFT) calculations.

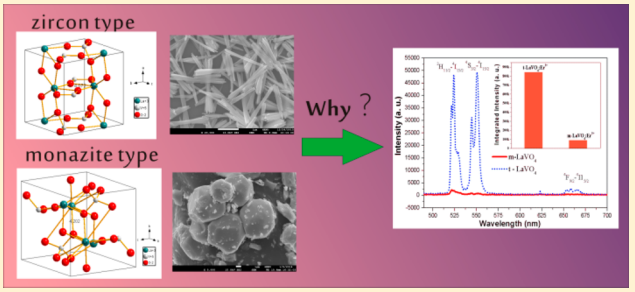

1. INTRODUCTION

Upconversion phosphors, which rely on the conversion of photons of lower energy to photons of higher energies, are attracting extensive interest in recent decades, owing to their superior features and a wide range of potential applications, such as background lighting source, solid-state lasers, infrared detection, and so on.[1,2] However, the upconversion luminescent materials are facing the question of low efficiency at the moment, which stringently limits their abundant applications. Thus, to effectively increase their efficiency is an important task for upconversion materials. Several ways have been reported to enhance the upconversion fluorescence efficiency, for instance, choosing suitable host materials, doping appropriate concentrations of lanthanide elements,[3] and impurity doping using Li^+.[4]

For high upconversion fluorescence efficiency, the fluoride crystals with low phonon energy can reduce the nonradiative loss and thus yield strong luminescence. Unfortunately, fluorides are usually hygroscopic and have less favorable chemical and photophysical stabilities compared with oxides' matrixes, and additionally, most of the preparative routes for Ln-doped halide-based upconversion nanoparticles are complex and often environmentally harmful.[5] In various oxides matrixes, lanthanide orthovanadates are potential hosts for luminescent materials. For instance, Yb^{3+} and Er^{3+}-codoped YVO_4 exhibit strong upconversion luminescence, which is comparable with the most efficient monoclinic $NaYF_4$:Yb^{3+}, Er^{3+} despite the phonon threshold for the bulk YVO_4 being as high as ~890 cm^{-1}.[6]

Among lanthanide orthovanadates, $LaVO_4$ exists in two phases, viz., monoclinic (m-) monazite type and tetragonal (t-) zircon type, with different reaction conditions. Generally, the larger La^{3+} prefers the monazite type due to its higher oxygen coordination number of 9 as compared to 8 of the zircon type; thus, the monazite type is the thermodynamically stable state.[7] The t-$LaVO_4$ has similar structure compared to that of YVO_4, which suggests that it is a promising candidate for phosphors. As expected, tetragonal zircon $LaVO_4$ is found to be a promising phosphor candidate as revealed by Shao et. al.[8] On the contrary, many reports confirm that m-$LaVO_4$ is neither a suitable host for luminescent activators nor a promising catalyst.[9,10] This attracts us to concentrate on the upconversion properties based on the host materials of both t- and m-$LaVO_4$.

For the preparation of monazite-type and zircon-type $LaVO_4$, thermodynamically stable m-$LaVO_4$ can be obtained by conventional solid-state reaction.[11] However, the main challenge lies in the synthesis of zircon-type $LaVO_4$ with

Received: April 15, 2015
Published: July 23, 2015

DOI: 10.1021/acs.inorgchem.5b00851
Inorg. Chem. 2015, 54, 7325−7334

higher crystallinity, which always means fewer traps and stronger luminescence,[12] because it is metastable and cannot be obtained by conventional methods.[13] The growth of zircon-type $LaVO_4$ has drawn much attention since the prior work by Ropp and Carroll in which they successfully synthesized the product via a precipitation method.[14] Later, the synthesis of t-$LaVO_4$ with high crystallinity by a hydrothermal method is reported by Oka et.al.,[15] and they claimed that the formation of t-$LaVO_4$ strongly depends on lanthanum and vanadium sources. Until the year 2004, Jia et. al reported that m- and t-phased $LaVO_4$ nanocrystals could be easily obtained by a hydrothermal method in a controllable way with additives such as EDTA.[16,17] Thereafter, the selective synthesis of m- and t-$LaVO_4$ nanocrystals are attracting extensive interest in studying phase-change processes and structure-dependent properties.[18−20] These works support easy and feasible ways to prepare the metastable t-$LaVO_4$.

Er^{3+} has relatively large energy gaps and thus low probabilities of nonradiative transitions among various excited levels of the ions. Therefore, it is a well-known activating ion for upconversion emission, and a great deal of research has involved Er^{3+} doping.[21−24] To enhance upconversion luminescence efficiency, a sensitizer with a sufficient absorption cross-section is usually codoped along with the activator to take advantage of the efficient energy-transfer upconversion process between the sensitizer and activator. In Er^{3+}-doped phosphors, Yb^{3+} ions are typically sensitizer because the absorption cross-section of Yb^{3+} ions in the NIR region is quite high compared to other lanthanide ions. Additionally, the $^2F_{7/2} \rightarrow {}^2F_{5/2}$ transition of Yb^{3+} is well resonant with f−f transitions of typical upconverting lanthanide ions such as Er^{3+}, Tm^{3+}, and Ho^{3+}, thus facilitating efficient energy transfer from Yb^{3+} to other ions. Moreover, the difference between ground state and excited state is approximately 10 000 cm^{-1}, which matches well with inexpensive 980 nm laser diodes as well as the $^4I_{11/2}$ excited intermediate state of the Er^{3+} ion.[25]

To the best of our knowledge, there is no report about upconversion luminescence properties of neither monazite-type nor zircon-type $LaVO_4$, although they have been considered as fascinating downshift luminescence properties.[26−28] Moreover, the phase transition significantly influencing the upconversion properties of phosphors has been reported. For example, hexagonal-phase $NaYF_4$:Yb^{3+}, Er^{3+} bulk materials exhibit about an order of magnitude enhancement of upconversion efficiency relative to their cubic phase counterparts.[29] However, basic research is lacking with respect to the reason for upconversion fluorescence properties dependent on the phases. On the basis of the above considerations, it is essential to study the upconversion luminescence properties on the basis of the hosts of both t- and m-$LaVO_4$ not only for developing novel upconversion materials but also for the basic reasons of the phase-dependent upconversion properties.

In this work, t-$LaVO_4$, Yb^{3+}/Er^{3+}-doped t-$LaVO_4$ were fabricated via a hydrothermal method, which has already been proven to be an effective way to synthesize metastable or novel compounds in high crystallinity. Furthermore, upconversion luminescence was demonstrated. In particular, we have given the explanation for the phase-dependent enhancement upconversion luminescence behavior using the crystal structures, electronic structures, Raman spectra, morphology, and crystal size. Finally, the results are intriguing not only for fundamental studies but also for the potential applications in many fields such as solar cells and optical thermometers.

2. EXPERIMENTAL AND COMPUTATIONAL DETAILS

2.1. Preparation. *(a) Samples Prepared via a Hydrothermal Synthesis Process.* Inspired by the work of Jia et al.,[16] we successfully synthesized t-$LaVO_4$ by the Na_2EDTA-assisted hydrothermal method. All the chemicals were of analytical grade and were used as received without further purification. First, a clear aqueous solution (solution a) of $La(NO_3)_3$, $Yb(NO_3)_3$, and $Er(NO_3)_3$ with a total of 2.5 mmol was obtained by dissolving La_2O_3 (99.99%), Yb_2O_3 (99.99%), and Er_2O_3 (99.99%) in dilute HNO_3 solution. Then, Na_2EDTA solid and Na_2EDTA/La^{3+} with a molar ratio of 1 were added to solution a under vigorous magnetic stirring to form solution b. Then, 2.5 mmol of $NH_4(VO_4)_3$ (99.6%) dissolved in 10 mL of heated deionized water was dripped into solution b to obtain solution c. The pH value of solution c was adjusted to 9 with 1 mol/L NaOH aqueous solution. Finally, a light yellow solution with a total volume of 70.0 mL was obtained. The mixed solution was transferred into a 100 mL Teflon autoclave, and then it was maintained at 180 °C for 12 h. The white precipitates were separated via centrifugation and washed with ethanol and deionized water. Lastly, it was dried in an oven at 60 °C for 24 h.

(b) Samples Obtained by a Solid-Reaction Method. Monazite-type $LaVO_4$ and $LaVO_4$:Yb^{3+}, Er^{3+} were prepared by a solid-state reaction from stoichiometric amounts of La_2O_3 (99.99%), $NH_4(VO_4)_3$ (99.6%), Yb_2O_3 (99.99%), and Er_2O_3 (99.99%). The stoichiometric mixtures were mixed and ground thoroughly and then were sintered in air at 900 °C for 12 h in a programmable furnace.

2.2. Characterization. The phase purity was recorded on a X-ray diffractometer (DX-2500, Fangyuan) with Cu Kα radiation (λ = 0.154145 nm) operating at 40 kV and 60 mA. The element analysis was performed on an inductively coupled plasma optical emission spectrometer (Optima 2100DV, PerkinElemer). The morphologies of the samples were observed by SEM (JSM-7001F, JEOL Ltd.). Further structural characterization was performed on a high-resolution field-emission transmission electron microscope (HRTEM) operating at 200 kV (JEM-2100, JEOL Ltd.) The chemical components were analyzed by FT-IR (Nicolet AVATAR360, Nicolet Company) and Raman (RM-1000, Renishaw) spectrometers. Upconversion emission measurements were performed using the HORIBA Jobin Yvon Fluorlog-3 Spectrofluorometer system using a continuous 980 nm laser diode with power maximum of 2W as the excitation source. Upconversion lifetimes were measured with a steady-state and phosphorescence lifetime spectrometer (FSP920-C, Edinburgh) equipped with a digital oscilloscope (TDS3052B, Tektronix) and a tunable midband Optical Parametric Oscillator (OPO) pulse laser as the excitation source. All the measurements were performed at room temperature. Thermogravimetric analysis (TGA) tests were performed under N_2 on an EXSTAR 6000 (Seiko Instrument Inc.) thermoanalyzer at a scanning rate of 10 °C/min.

2.3. Computational Details. The initial structures of pure t-$LaVO_4$ or m-$LaVO_4$ were constructed on the basis of the structural information reported in refs 15 and 30, respectively. For Er^{3+} doping of t- or m-$LaVO_4$, we used a 2 × 1 × 1 t- or m-$LaVO_4$ supercell containing 48 atoms in which a La atom was substituted with a Er atom to simulate Er^{3+} element doping.

The electronic structures were calculated via two steps. First, the structures were optimized using the Vienna ab initio simulation package (VASP).[31] For the exchange−correlations functional, the generalized-gradient approximation (GGA) of Perdew et al.[32] was used. The cutoff kinetic-energy is set to be 500 eV. For the Brillouin zone integration, a 9 × 11 × 8 or 5 × 9 × 11 Monkhorst−Pack special k points grid was used for pure and Er doping samples, respectively.

An accurate description for electronic structures is by the full-potential linearized augmented plane waves (FLAPW) method implemented in the WIEN2k.[33,34] The exchange−correlation potential is Engel−Vosko with generalized-gradient approximation (EV-GGA).[35] A cutoff parameter $R_{mt} \times K_{max}$ = 7 and a nonshifted mesh with 1000 k or 500 k points, respectively, are used for pure and Er^{3+} doping cases.

DOI: 10.1021/acs.inorgchem.5b00851
Inorg. Chem. 2015, 54, 7325−7334

3. RESULTS AND DISCUSSION

3.1. Structure and Morphology Analysis. The crystal structure of $LaVO_4$ presents two phases, zircon and monazite, depending on the different experimental conditions. The crystal phases of all the products were detected by XRD. Figure 1a shows the XRD patterns of the t-$LaVO_4$:1%Er^{3+}, t-$LaVO_4$:10% Yb^{3+}, 1%Er^{3+}, respectively, marked as S1 and S2 prepared by a hydrothermal method, and m-$LaVO_4$:1%Er^{3+} noted as S3 synthesized via a solid-state reaction method. It is shown that S1 and S2 can be well indexed to the t-$LaVO_4$ (JCPDS file no. 32-0504), and the patterns of S3 matches well with standard m-$LaVO_4$ (JCPDS file no. 50-0367), which reveals that the reaction condition is a key factor affecting the crystal phase of the products. The crystal structures of the two phases, t- and m-$LaVO_4$ were, respectively, given as panels b and c on the right of Figure 1. Regarding t-$LaVO_4$ with the *I*4/*amd* space group, La atom coordinated with eight oxygens to form a LaO_8 dodecahedron occupies D_{2d} sites of the higher symmetry environment. For m-$LaVO_4$ with the *P*2/*n* space group, La atom, which is to be coordinated by nine oxygens forming an irregular LaO_9 polyhedron, occupies C_1 symmetry environment.[15,30] The nearest distance of La−La is 4.072 Å for t-$LaVO_4$ whereas it is 4.202 Å for m-$LaVO_4$.

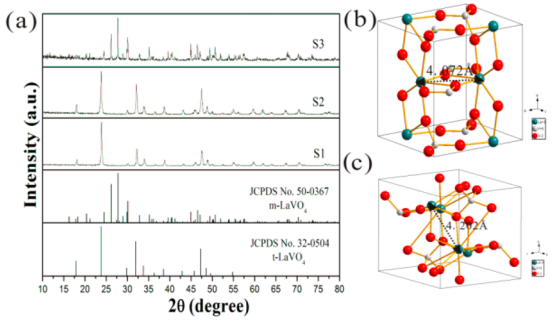

Figure 1. (a) XRD patterns of (S1) t-$LaVO_4$:1%Er^{3+}, (S2) t-$LaVO_4$:10%Yb^{3+},1%Er^{3+}, and (S3) m-$LaVO_4$:1%Er^{3+}. The standard XRD patterns of JCPDS files no. 32-0504 (t-$LaVO_4$) and no. 50-0367 (m-$LaVO_4$) are also shown. (b) and (c) represent the crystal structures of t-$LaVO_4$ and m-$LaVO_4$, respectively.

The doping concentration of rare earth ions strongly depends on the preparation condition especially for the hydrothermal process.[36] To get the relative precise amounts on the doping content of Er, ICP-OES was employed to analyze the products. The results of element content are listed in Table 1. The results indicate that Er is, respectively, 0.33% and 0.36% for the t-$LaVO_4$:1%Er^{3+} and m-$LaVO_4$:1%Er^{3+} samples.

The presence of quenching groups of the sample would affect the luminescence property. To further determine the chemical composition of the product prepared via the hydrothermal method, FT-IR spectroscopy of t-$LaVO_4$ was carried out, and the result is shown in Figure 2. The spectrum exhibits a weak peak at 441 cm^{-1} and a main absorbable peak in the range of 720−980 cm^{-1}, respectively, corresponding to the characteristic vibrational mode of the La−O bond and the V−O bond (from the VO_4^{3-} group), and the peak at 1390 cm^{-1} is associated with the N−O bond from NO_3^- groups.[37] The weak bands at 2850 and 2923 cm^{-1} can be assigned to the asymmetric and symmetric stretching vibrations of the $-CH_2$ in the remaining Na_2EDTA. The smaller one at 1629 cm^{-1} and the broad band at 3429 cm^{-1} are corresponding to the OH groups of H_2O absorbed on the surface of t-$LaVO_4$.[38]

Table 1. ICP Results of the t-$LaVO_4$:1%Er^{3+} and m-$LaVO_4$:1%Er^{3+} Samples

	t-$LaVO_4$:1%Er^{3+}	m-$LaVO_4$:1%Er^{3+}
molar ratio of La:V	1.01:1	0.95:1
Er^{3+} content (mol %)	0.33	0.36

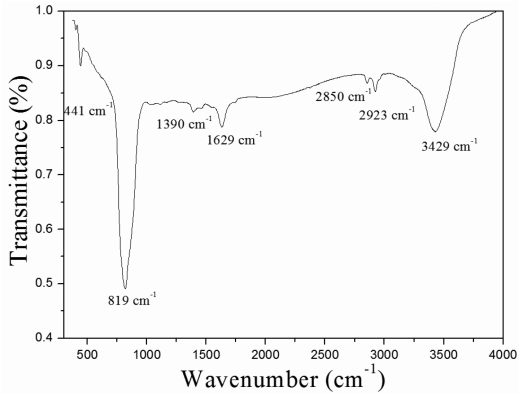

Figure 2. FTIR spectrum of t-$LaVO_4$ sheaf-like microcrystals.

Figure 3 shows the SEM images of t-$LaVO_4$ and m-$LaVO_4$. (a) and (b) show that the product t-$LaVO_4$ looks like strawsheaves with two fantails consisting of a bundle of outspread nanorods bonding in the middle. The morphology has also been observed in other lanthanide orthovanadates such as $CeVO_4$.[39] The average diameter of the nanorods is 70 nm, and the individual strawsheaf has an average length of about 2.4 um. (c) and (d) indicate that a large proportion of m-$LaVO_4$ particles presents spherical-like structures with diameter ranging from 4 to 7 um which is much larger than that of t-$LaVO_4$.

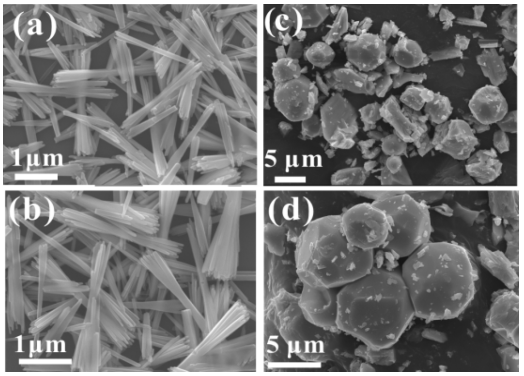

Figure 3. (a) and (b) SEM images of t-$LaVO_4$ prepared at 180 °C for 12 h via hydrothermal synthesis, (c) and (d) SEM images of as-obtained m-$LaVO_4$.

3.2. Possible Formation Mechanism. As an important organic additive, Na_2EDTA has strong coordination ability with La^{3+} to form certain intermediate complexes.[40] To determine the crystal growth process and the assembly of the sheaf-like microcrystals, we conducted time-dependent experiments by keeping other reaction parameters unchanged. Figure 4 shows the SEM images of $LaVO_4$:Yb^{3+}, Er^{3+} (Na_2EDTA/La^{3+} = 1:1, pH = 9) prepared at 180 °C for different reaction times.

DOI: 10.1021/acs.inorgchem.5b00851
Inorg. Chem. 2015, 54, 7325−7334

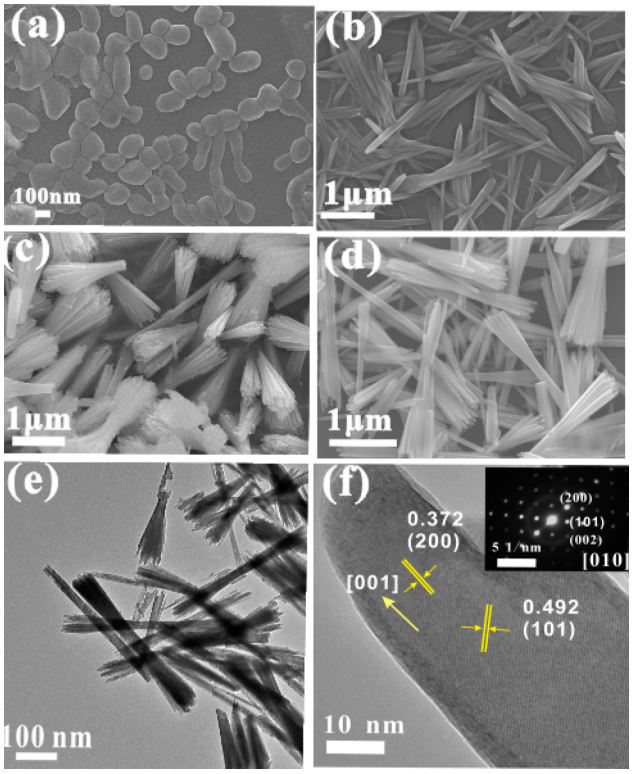

Figure 4. SEM images of evolution for t-$LaVO_4$ prepared at different hydrothermal times, (a) 10 min, (b) 30 min, (c) 4 h, and (d) 12 h. (e) TEM images, and (f) HRTEM images and corresponding electron diffraction pattern of t-$LaVO_4$ prepared at 180 °C, 12 h.

First, the relatively stable coordination complex $(LaEDTA)^-$ was formed by chemically bonding between Na_2EDTA and La^{3+}. Under hydrothermal treatment, the initial colloidal $LaVO_4$ nuclei was formed, and $EDTA^{2-}$ ions were released due to reaction between the $(LaEDTA)^-$ complexes and VO_4^{3-}. Thus, nanoparticles with wide particle size distribution of 60−200 nm and irregular morphology are found as shown in Figure 4a. Then, the colloidal $LaVO_4$ nuclei can be mediated by the adsorbed $EDTA^{2-}$ ligand on the $LaVO_4$ surface, and through the interaction, the free energies of different facets would be changed. Then, the initial nuclei serve as seeds for the growth of highly anisotropic nanostructure in the solution-solid process via the dissolution and crystallization mechanism.[41] Subsequently, the long rod-like structures with various lengths can be detected with the increase of the reaction time to 30 min (Figure 4b). Moreover, Na_2EDTA can cap the side walls of the nanorods in the fantails of the strawsheaves due to the characteristic of its hydrophile, which has been mentioned before.[39] As for the sample prepared with reaction time of 4 and 12 h (Figure 4c and d), the tails of the strawsheaves have fanned out, leading the nanocrystal splitting to form sheaves or even double-headed broccoli-like spherulites of $LaVO_4$. The origin of the crystal splitting has been explained previously.[20] To further understand the fine structure of the strawsheaves, TEM and HRTEM images are also shown in Figure 4e,f. The electron-diffraction pattern given in the inset of Figure 4f indicates the single-crystalline nature of the nanorods. The clear lattice fringes in the HRTEM images confirm the high crystallinity of the rods. The measured adjacent lattice spacings of the nanorods are about 0.372 and 0.492 nm, which is consistent with the interplanar spacing of the (200) and (101) facets of t-$LaVO_4$, respectively. The close observation of the HRTEM image indicated that (200) facets are parallel to the side planes. Furthermore, the corresponding ED pattern has been indexed. The spots could be assigned to the (200), (101), and (002) facets. Combining the HRTEM image and the corresponding ED pattern, it can be noticed that the [001] direction is vertical to the side plane of the rods. These observation suggests the growth of the nanorods along the [001] direction.

On the basis of the above results, the possible formation mechanism as well as the crystal dimension evolution process of the nanostructures is proposed in Scheme 1.

Scheme 1. Schematic Illustration of the Growth Process of $LaVO_4$ Using Na_2EDTA as Additive

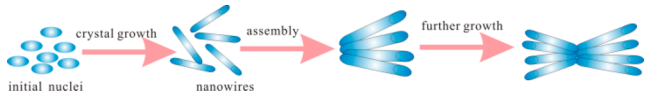

3.3. Upconversion Luminescence Properties.

Figure 5 displays the upconversion emission spectra of zircon-type and

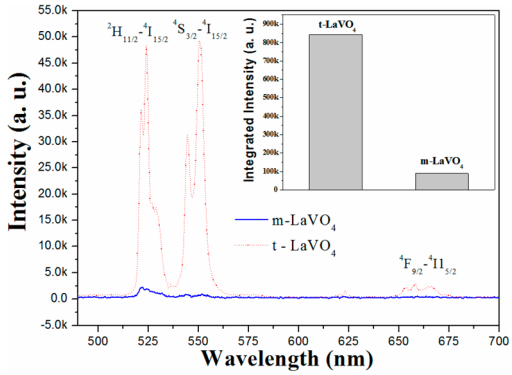

Figure 5. Room temperature upconversion spectra of t-$LaVO_4$:1%Er^{3+} and m-$LaVO_4$:1%Er^{3+} at 980 nm excitation. The inset gives their integrated intensity.

monazite-type bulk $LaVO_4$:Er^{3+} with a doping level of 1 mol % Er^{3+} under the excitation of 980 nm laser diodes at 228 mW. Both of them consist of three emission peaks around 525, 548, and 670 nm which are, respectively, attributed to $^2H_{11/2}-^4I_{15/2}$, $^4S_{3/2}-^4I_{15/2}$, $^4F_{9/2}-^4I_{15/2}$ transitions of Er^{3+}. The shorter-wavelength emissions at 525 and 548 nm are predominated and much more intense than the long-wavelength emission at 670 nm. The much stronger emissions at 525 and 548 nm are in accordance with the green-emitting color as observed. The energy gaps between $^4S_{3/2}$ and $^4F_{9/2}$, $^4I_{11/2}$ and $^4I_{13/2}$ are about 3000 and 3600 cm^{-1}, respectively.[42] The phonon energy of both the zircon and monazite $LaVO_4$ system is determined to be around 860 cm^{-1} from the discussion of Raman spectra below. Thus, nonradiative relaxation processes of $^4S_{3/2} \rightarrow {}^4F_{9/2}$ and $^4I_{11/2} \rightarrow {}^4I_{13/2}$ levels request a few phonon energies to bridge the energy gap according the energy gap law. Therefore, the nonradiative relaxation processes are inefficient, resulting in the relatively strong green emission peak. It is worthwhile to note that the emission intensity of zircon-type $LaVO_4$:Er^{3+} is much higher (about 10 times) than that of monazite-type $LaVO_4$:Er^{3+}, even though a smaller doping level of Er^{3+} presents in zircon-type $LaVO_4$ detected by ICP-OES. To better show the relationship of the intensity, the inset of Figure 5 was also

DOI: 10.1021/acs.inorgchem.5b00851
Inorg. Chem. 2015, 54, 7325−7334

given. This phenomenon attracts us to understand the real reason for the purpose of supplying basic data to develop novel efficient upconversion materials. Actually, there are two main factors influencing the luminescence intensities: crystal structure including phonon energy, the distance between luminescence centers, and both morphology and size.

From the analysis of crystal structures before, the local structure of the rare-earth ions in t-$LaVO_4$ and m-$LaVO_4$ is different, which can affect electronic transition probabilities determining the luminescence intensity. This has been proved by the work in ref 17. However, it is lacking of basic data to reveal the effect of the local structure on electronic transition probabilities. The electronic transition is related to the electronic structures. Thus, we study the electronic structures of $LaVO_4$ and Er^{3+} doping for the sake of understanding the reason for the enhanced upconversion. The electronic band structures for the pure t or m-$LaVO_4$ and Er^{3+} doping t or m-$LaVO_4$ along high symmetry directions are shown in Figure 6.

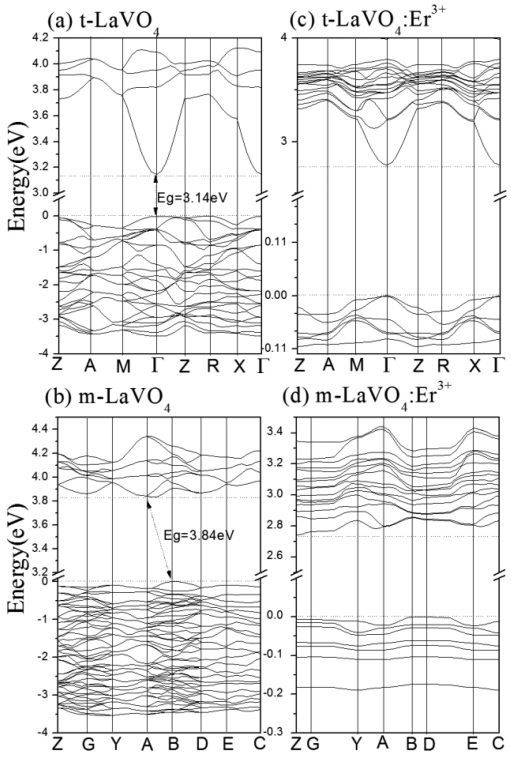

Figure 6. Band structure plots for pure t-$LaVO_4$ (a) and m-$LaVO_4$ (b), Er-doped t-$LaVO_4$ (c) and m-$LaVO_4$ (d).

Figure 6a exhibits that the valence band maximum as well as the conduction minimum is located at the Γ point, indicating that t-$LaVO_4$ is a direct band gap material with a band gap of 3.14 eV. As seen from the electronic band structure of m-$LaVO_4$ shown in Figure 6b, the valence band maximum is located at the A point and the conduction minimum is situated at the B point. Unlike t-$LaVO_4$, m-$LaVO_4$ is an indirect band gap material with a band gap of 3.84 eV. The case of the larger band gap of m-$LaVO_4$ compared to t-$LaVO_4$ accords with the reported trend in ref 43. The obtained values are close to the experimental values for t-$LaVO_4$ (3.18 eV)[44] and m-$LaVO_4$ (3.5 ± 0.2 eV)[45] measured from optical absorption edge, which confirms the reliability of our calculations. These large band gaps indicate that both phases of $LaVO_4$ are insulators.

The doping cases for t-$LaVO_4$ and m-$LaVO_4$ are illustrated in Figure 6c,d. For m-$LaVO_4$:Er^{3+} which has the $P2/n$ space group, Er^{3+} would occupy the C_1 symmetry environment. Whereas for t-$LaVO_4$:Er^{3+} with $I4/amd$ space group, Er^{3+} would occupy the D_{2d} site higher symmetry environment. The difference lattice sites of the luminescence center can lead to the distinct band structures. Comparison between doping cases with pure cases indicated that a narrow band appears for the two cases arising from the localized Er f orbitals, which will be confirmed by density of states. Comparing the two doping cases, we found that the band of t-$LaVO_4$:Er^{3+} rising from localized Er f near 0 eV is much more dispersive than that of m-$LaVO_4$:Er^{3+}. The different dispersion is probably related to the fact that the local structure of Er^{3+} in t-$LaVO_4$ is different compared to that of m-$LaVO_4$. Large band dispersions, which decrease the effective masses of electrons and holes, ensure a fair mobility of the photoinduced charge carriers. Therefore, the larger band dispersions of Er f states, viz., the less-localized nature of the Er f orbital, supply the possible condition that leads to excellent upconversion fluorescence.

To investigate the source of the electron states near the band edges, the contributions from each of the related orbitals to total density of states for pure $LaVO_4$ and Er^{3+} doping $LaVO_4$ are displayed by partial density of states (DOS) in Figure 7.

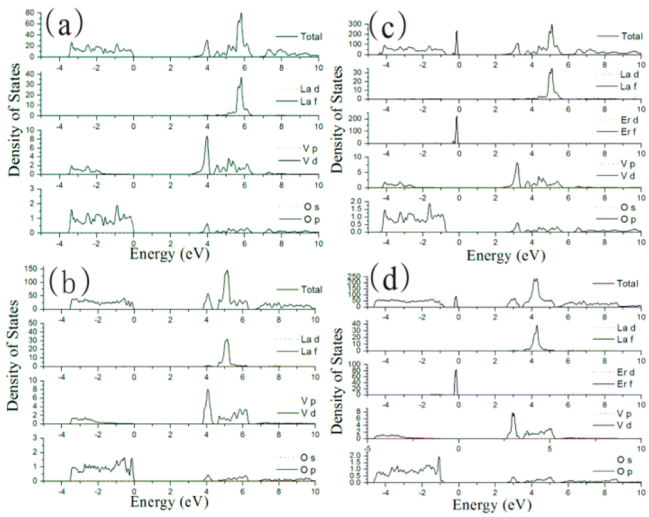

Figure 7. Density of states plots and partial density of states for pure t-$LaVO_4$ (a) and m-$LaVO_4$ (b), Er-doped t-$LaVO_4$ (c) and m-$LaVO_4$ (d).

From Figure 7, the two pure cases exhibit some similar features. It can be seen that the upper valence band between −4.0 eV and the Fermi level (0.0 eV) was dominated by O s and V d states. The large overlapping between O s and V d states indicates the covalent bonding character. Turning to the conduction band, it mainly consists of V d and La f states just above the Fermi level, with some contributions of the O s states. To assign the bands of the doping cases in Figures 6b,d, the total and partial densities of states are depicted in Figure 7b,d. For the two doping cases, the energy bands between −4 and −0.5 eV are dominated by O s and V d states, and the conduction band has been contributed by V d and La f states, with some contributions of the O s states. It is difficult, however, to recognize the small fraction of Er f in the conduction band in Figure 7 because of the stronger peak of Er f in the valence band. Comparing the two doping cases, the

DOI: 10.1021/acs.inorgchem.5b00851
Inorg. Chem. 2015, 54, 7325−7334

region covered by Er f for t-$LaVO_4$ is broader than that of m-$LaVO_4$. Actually, the bandwidth is mainly determined by the extent to which orbitals on neighboring atoms overlap. Therefore, the different bandwidth of Er f orbital suggests the different local structure of Er^{3+} in the two phases. This result accords with the crystal structures of t-$LaVO_4$ and m-$LaVO_4$ as well as the phenomenon from the observation of band structures.

Furthermore, the ratio of integrated DOS in the energy windows of −0.4−0 eV from the VB top to total electrons is 4% and 2% for Er-doped t-$LaVO_4$ and m-$LaVO_4$, respectively. The larger DOS in the VB around the Fermi Energy E_F implies an increase of charge carriers of t-$LaVO_4$ than that of m-$LaVO_4$. This will lead to a higher transition from the ground state of Er. The experimental observation is consistent with the theoretical prediction. On the basis of the analysis above, the different local structure of Er^{3+} affecting electronic transition probabilities is considered an important reason for the disparity of emission intensity.

It has been reported that the involvement of large phonon models effectively bridged some nonradiative relaxation channels, which could induce the decreasing of luminescence efficiency. A low phonon energy is a benefit for the high upconversion efficiency of the product.[3] The information from Raman spectra was employed to characterize the phonon energies. The Stokes Raman spectra (λ_{ex} = 532 nm) of t-$LaVO_4$ and m-$LaVO_4$ hosts, which did not contain rare earth dopants to prevent their photoluminescence from obscuring the much weaker Raman signal, are shown in Figure 8. From the two

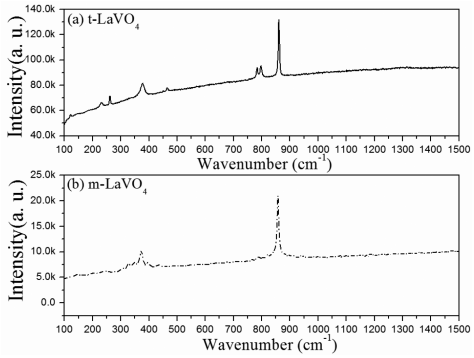

Figure 8. Raman spectra of (a) t-$LaVO_4$ and (b) m-$LaVO_4$.

spectra, two parts are clearly observed, containing the high-energy part between 745 and 880 cm^{-1} and the low-energy part below 480 cm^{-1}. The former vibration peaks correspond to the "internal" vibrations of the tetrahedral VO_4 group, and the latter part mainly originates from the La−O vibrations.[16]Com-Comparing the two spectra, the number of vibration peaks in the low-energy region assigned to La−O vibration peaks below 480 cm^{-1} is quite different due to the different structures between t- and m- $LaVO_4$. The number of vibration peaks for t-$LaVO_4$ is smaller than that for m-$LaVO_4$. The decreased number of vibration peaks for t-$LaVO_4$ is in accordance with the lower coordination number (8) and the high symmetry (D_{2d}) of the La^{3+} ions which have been indicated before. A strong Raman peaks for t-$LaVO_4$ is around 861 cm^{-1}, whereas that for m-$LaVO_4$ is around 858 cm^{-1}. This indicates the main phonon energy of t-$LaVO_4$ is slightly higher than that of m-$LaVO_4$ in our case. However, we cannot estimate the presence of larger phonon modes such as −OH via Raman technology. The similar value of the main phonon energy suggests that it is not the key reason influencing the luminescence intensities between t-$LaVO_4$:Er^{3+} and m-$LaVO_4$:Er^{3+}.

It is well-known the luminescent intensity is also related to the average distance between luminescent centers. Before the dopant-ion concentration reaches a certain level, the short distance between active ions will increase the upconversion luminescence. From the structure analysis in Figure 1, the nearest distance of La−La is for t-$LaVO_4$ (4.072 Å), which is close to that for m-$LaVO_4$ (4.202 Å). Thus, we considered that it is also not a main factor resulting in the large difference of luminescence intensity. Usually, the sample with high crystallinity and a large crystal size exhibit higher luminescence intensity. However, both the samples have good crystallinity from the results of XRD patterns. In addition, the scale of monazite-type $LaVO_4$:Er^{3+} is much larger than that of zircon type from SEM photograph. Therefore, the good crystallinity and larger crystal size of m-$LaVO_4$:Er^{3+} are not in accordance with the lower emission intensity. According to the analysis above, it is safe to consider that the different local structure of Er^{3+} is a key reason for the disparity of emission intensity in our case.

Yb^{3+} is often used as a sensitizer for Er^{3+} because of the low absorption cross section of Er^{3+} in the NIR range. As expected, the emission intensity at 525, 548, and 670 nm, respectively, attributed to $^2H_{11/2}$−$^4I_{15/2}$, $^4S_{3/2}$−$^4I_{15/2}$, $^4F_{9/2}$−$^4I_{15/2}$ transitions of Er^{3+} was enhanced when Yb^{3+} ions were doped into t-$LaVO_4$:1%Er^{3+} and m-$LaVO_4$:1%Er^{3+}, which is obtained after comparing both the intensities of t/m-$LaVO_4$:1%Er^{3+} and t/m-$LaVO_4$:10%Yb^{3+}, 1%Er^{3+}. To study the mechanism of upconversion luminescence, Figure 9 displays the upconversion

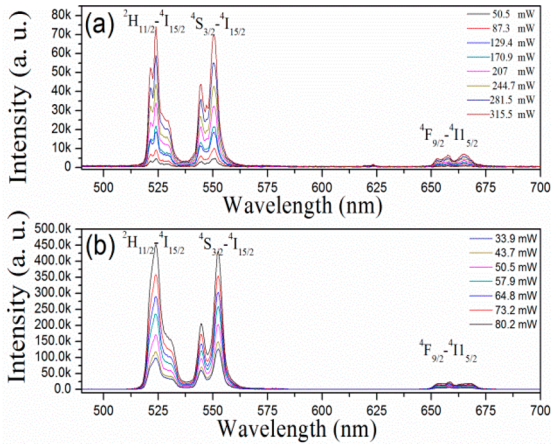

Figure 9. Dependence of upconversion emission intensity of t-$LaVO_4$:10%Yb^{3+}, 1%Er^{3+} (a) and m-$LaVO_4$:10%Yb^{3+}, 1%Er^{3+} (b) on excitation power.

emission spectra of t- and m-$LaVO_4$:10%Yb^{3+}, 1%Er^{3+} under laser diode excitation of 980 nm at various pump powers. From the spectra, it is obvious that the emission intensities of the two samples become stronger with enhanced pump powers.

3.4. Upconversion Mechanism. To understand the populating mechanism of the $^2H_{11/2}$, $^4S_{3/2}$, and $^4F_{9/2}$ excited states under irradiation of NIR light, the intensities of green and red emissions as a function of the excitation power were measured, as shown in Figure 10. It is well-known that the relationship is expressed as

DOI: 10.1021/acs.inorgchem.5b00851
Inorg. Chem. 2015, 54, 7325−7334

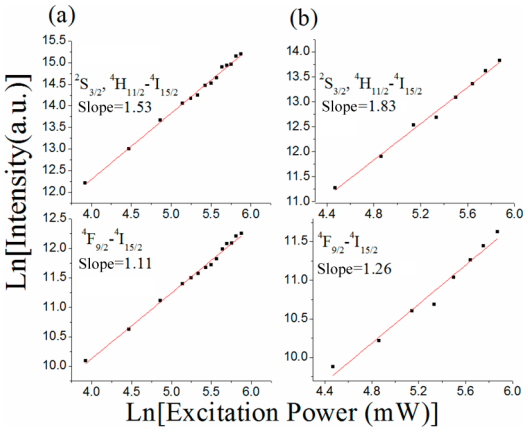

Figure 10. Dependence of the intensities of the green and red emissions on the excitation power (a) t-$LaVO_4$:1%Er^{3+}, (b) t-$LaVO_4$:10%Yb^{3+}, 1%Er^{3+}.

$$I_{uc} \propto I_{pump}{}^{n} \text{ with } n = 1, 2, 3 .... \quad (1)$$

where n is the number of photons required to populate the visible emitting states. For the sample t-$LaVO_4$:1%Er^{3+}, by fitting the data points, the slopes for the ($^2H_{11/2}$, $^4S_{3/2}$)-$^4I_{15/2}$ and $^4F_{9/2}$-$^4I_{15/2}$ transitions are 1.53 and 1.11, respectively. In Yb^{3+} and Er^{3+}-codoped t-$LaVO_4$, slopes of 1.83 and 1.26 respective for the ($^2H_{11/2}$, $^4S_{3/2}$)-$^4I_{15/2}$ and $^4F_{9/2}$-$^4I_{15/2}$ transitions can be obtained by fitting the data points. The corresponding results are shown in Figure 8a,b. As for m-$LaVO_4$:Yb^{3+}, Er^{3+}, we obtained the similar fitting results. The slops for ($^2H_{11/2}$, $^4S_{3/2}$)−$I_{15/2}$ and $^4F_{9/2}$−$^4I_{15/2}$ transitions are respectively 1.21 and 1.01 in m-$LaVO_4$:1%Er^{3+}, and respectively 2 and 1.75 in m-$LaVO_4$:10%Yb^{3+}, 1%Er^{3+}. From the results, a two-photon process is involved to green and red emissions for both t/m-$LaVO_4$:1%Er^{3+} and t-m $LaVO_4$:10%Yb^{3+}, 1%Er^{3+}. The calculated slope value being lower than the expected value is due to the saturation in the upconversion process at higher power as well as the local thermal effect, which have been previously reported.[36,46]

In order to better describe the upconversion behavior of t-$LaVO_4$:Yb^{3+}, 1%Er^{3+} and m-$LaVO_4$:Yb^{3+}, 1%Er^{3+}, the Yb^{3+} concentration-dependent upconversion luminescence spectra of both t-$LaVO_4$:Yb^{3+}, 1%Er^{3+} and m-$LaVO_4$:Yb^{3+}, 1%Er^{3+} are shown in Figure 11. It has been reported that the variation of

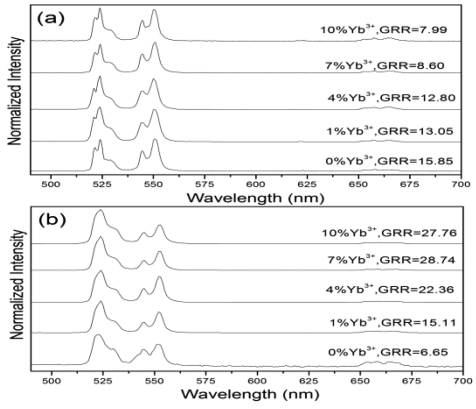

Figure 11. Yb^{3+} concentration-dependent upconversion luminescence properties of (a) t-$LaVO_4$:Yb^{3+},1%Er^{3+} and (b) m-$LaVO_4$:Yb^{3+}, 1% Er^{3+}.

GRR (i.e, the G/R emission intensity) depends not only on the radiative transition and nonradiative transition process but also strongly on the cross-relaxation process.[1] These processes are very important to understand upconversion process.

From the GRR data, it can be concluded that (1) the GRR of t-$LaVO_4$:1%Er^{3+} is larger than that of m-$LaVO_4$:1%Er^{3+}. Actually, besides radiative transition, there are mainly two upconversion population channels affecting the GRR, one is the nonradiative relaxation of $^4F_{7/2}$−$^2H_{11/2}$/$^4S_{3/2}$, $^4S_{3/2}$−$^4F_{9/2}$, and $^4I_{11/2}$−$^4I_{13/2}$, the other is the cross-relaxation of $^4F_{7/2}$+$^4I_{11/2}$−$^4F_{9/2}$+$^4F_{9/2}$. The nonradiative relaxation of $^4S_{3/2}$−$^4F_{9/2}$ and $^4I_{11/2}$−$^4I_{13/2}$ (via the route $^4I_{11/2}$+$^4I_{13/2}$−$^4I_{15/2}$+$^4F_{9/2}$) and cross-relaxation of $^4F_{7/2}$+$^4I_{11/2}$−$^4F_{9/2}$+$^4F_{9/2}$ contribute to the red level population while $^4F_{7/2}$−$^2H_{11/2}$/$^4S_{3/2}$ leads to the green emission. Therefore, the ratio of G/R depends on the competition between $^4F_{7/2}$−$^2H_{11/2}$/$^4S_{3/2}$, and $^4S_{3/2}$−$^4F_{9/2}$, $^4I_{13/2}$−$^4I_{11/2}$ or $^4F_{7/2}$+$^4I_{11/2}$−$^4F_{9/2}$+$^4F_{9/2}$. In t-$LaVO_4$:1%Er^{3+}, because of the reside of the large phonon modes such as −CH_2 and OH− bonds, the nonradiative relaxation from $^2H_{11/2}$/$^4S_{3/2}$ to the red level $^4F_{9/2}$ should be increased, which results in the decrease of GRR. However, the experiment result is the converse. Thus, it is not the main reason. From the SEM images of t and m-$LaVO_4$, the straw-like t-$LaVO_4$ is composed of nanorods. The boundary effect of nanorods will suppress the cross-relaxation among Er^{3+}. In addition, the actual doping level of Er^{3+} is lower in t phase. The low level will prevent the formation of Er^{3+} clusters, finally affecting the cross-relaxation. These facts will induce the larger GRR of t-$LaVO_4$:1%Er^{3+}. (2) As the concentration of Yb^{3+} increases, the ratio of G/R tends to decrease for t-$LaVO_4$:Yb^{3+}, Er^{3+}, while in m-$LaVO_4$:Yb^{3+}, Er^{3+} it increases initially until that the concentration of Yb^{3+} reaches 7% and subsequently slightly decreases. The varies of GRR indicates that the intermediary level in the red channel population is different from $^4I_{11/2}$,[47] for favorable energy matching, the red level population route involves the $^4I_{13/2}$ level via $^4F_{5/2}$(Yb^{3+})+$^4I_{13/2}$(Er^{3+})−$^2F_{5/2}$(Yb^{3+})+$^4F_{9/2}$ (Er^{3+}).

In t-$LaVO_4$:Yb^{3+}, Er^{3+}, the large phonon modes in t-$LaVO_4$ will increase the probability of the nonradiative relaxation of $^4S_{3/2}$−$^4F_{9/2}$ and $^4I_{11/2}$−$^4I_{13/2}$. Meanwhile, more Er^{3+} will be excited to excited sates with the increasing of the amounts of Yb^{3+} including the $^4I_{13/2}$−$^4F_{9/2}$ transition, which contributes to the red level population route and reduces the GRR. As for m-$LaVO_4$:Yb^{3+}, Er^{3+}, the probability of nonradiative relaxation of $^4S_{3/2}$−$^4F_{9/2}$ and $^4I_{11/2}$−$^4I_{13/2}$ is low to affect GRR, but the cross-relaxation among Er^{3+} is an important reason for red emission. With increasing the concentration of Yb^{3+}, the cross-relaxation among Er^{3+} will be prevented gradually because of the energy-transfer upconversion (ETU) process between Yb^{3+} and Er^{3+}. Thus, the ratio of G/R is increased initially. Finally, with 10 mol % doping, a slight decrease of GGR which is likely caused by the concentration quenching.[48]

Furthermore, to understand upconversion luminescence behavior in t- and m-$LaVO_4$:Er^{3+} samples, the dynamic processes of the excited states ($^4S_{3/2}$ and $^4F_{9/2}$) for Er^{3+} ions in t-$LaVO_4$:1%Er^{3+} and m-$LaVO_4$:1%Er^{3+} samples were measured and compared under the excitation of 980 nm, which is shown in Figure 12. For the $^4S_{3/2}$−$^4I_{15/2}$ transition of t-$LaVO_4$:1%Er^{3+}, the decay of the emission intensities is nearly biexponential, which can be written as

$$I(t) = I_1\exp(-t/\tau_1) + I_2\exp(-t/\tau_2) \quad (2)$$

DOI: 10.1021/acs.inorgchem.5b00851
Inorg. Chem. 2015, 54, 7325−7334

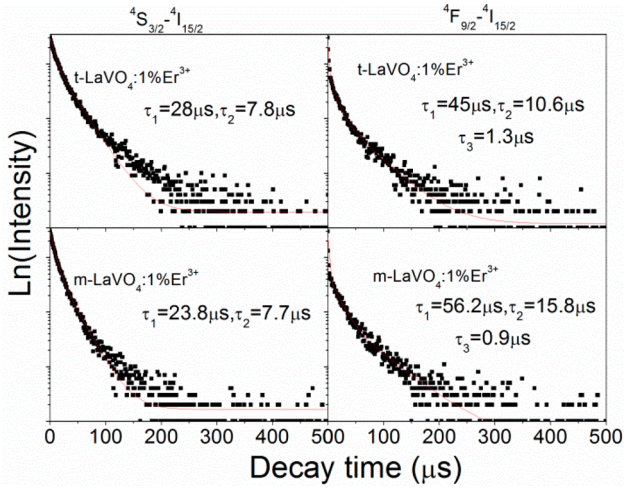

Figure 12. Typical dynamic processes of the $^4S_{3/2}$−$^4I_{15/2}$ and $^4F_{9/2}$−$^4I_{15/2}$ transitions of Er^{3+} in t-$LaVO_4$:1%Er^{3+} and m-$LaVO_4$:1% Er^{3+}samples.

where τ_1 and τ_2 represent the shorter and longer lifetime constants, respectively, and I_1 and I_2 are the original contribution for the shorter and longer decay times, respectively. It is suggested that the appearance of biexponential decay processes comes from the emissions of Er^{3+} ions at different local environments.[49] In our case, the shorter process should be attributed to the emissions of Er^{3+} ions on the surface of nanorods, while the longer process are relative with Er^{3+} ions at inner sites of crystals. As for m-$LaVO_4$:1%Er^{3+}, the upconversion luminescence of $^4S_{3/2}$−$^4I_{15/2}$ also decays double exponentially. The double exponent behavior may involve isolated and clustered Er^{3+} sites.[50] The details are under investigation in our further work. The $^4F_{9/2}$−$^4I_{15/2}$ transition in both t- and m-$LaVO_4$:Er^{3+} decays multiexponentially, which suggests the involving of $^4I_{13/2}$ level and cross-relaxation among Er^{3+} in the samples.

On the basis of the discussion above, typical energy diagrams and the possible mechanism for the upconversion luminescence for Er^{3+}-doped and Yb^{3+}, Er^{3+}-codoped samples were given in Figure 13a,b, respectively. In Er^{3+} single-doped system, upconversion processes contain the excited-state absorption (ESA) process and ETU process. The mechanism for ESA is comparatively simple. Er^{3+} is first excited from the $^4I_{15/2}$ level to

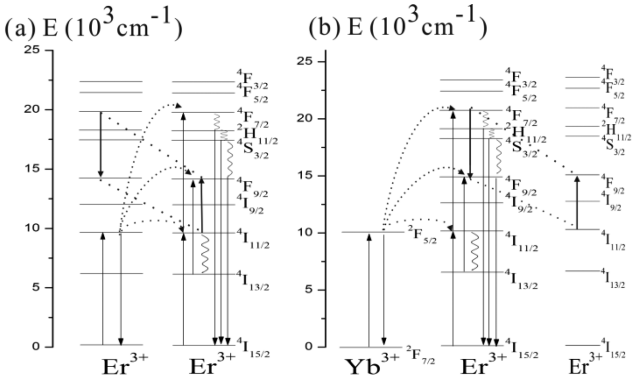

Figure 13. Simplified energy-level diagrams of (a) Er^{3+}, and (b) Er^{3+}, Yb^{3+} and the possible mechanism for the upconversion luminescence. The solid, dotted, and curve represent the radiative, energy transfer, and multiphoton relaxation processes, respectively.

the $^4I_{11/2}$ level, and then to the $^4F_{7/2}$ level by the absorption the energy of a second photon from the incident laser beam. The state is unstable, and thus, the ions on the $^4F_{7/2}$ level decay nonradiatively to $^2H_{11/2}$, $^4S_{3/2}$, and $^4F_{9/2}$ levels. Alternatively, after initial excitation, the Er^{3+} on the $^4I_{11/2}$ level can decay nonradiatively to the $^4I_{13/2}$ level and then populates the $^4F_{9/2}$ level by the absorption of a second 980 nm wavelength photon. In the ETU process, which is dominant at higher concentrations of Er^{3+} ions,[51] two excited Er^{3+} ions on the $^4I_{11/2}$ level interact with each other. One Er^{3+} ion transfers its energy to the neighboring ion, leaving it in the higher excited state $^4F_{7/2}$, and nonradiatively decays back to the ground state. Besides, from the analysis above, the cross relaxation of $^4F_{7/2}$+$^4I_{11/2}$−$^4F_{9/2}$+$^4F_{9/2}$ is the possible route to populate the red level $^4F_{9/2}$. For the emission process, the $^4F_{9/2}$, $^4S_{3/2}$, and $^2H_{11/2}$ levels depopulate to the ground state emitting 662, 551, and 524 nm lights, respectively.

For Yb^{3+}, Er^{3+}-codoped sample, first, Er $^{3+}$ ions on $^4I_{15/2}$ are excited to $^4I_{11/2}$ by the ground state absorption (GSA) and/or energy transfer of Yb^{3+} −Er $^{3+}$. Then the same laser pumps the excited state electrons from the $^4I_{11/2}$ to the $^2H_{11/2}$ levels via ESA or the second-step ET of Yb^{3+} −Er $^{3+}$, the electrons relax to $^4S_{3/2}$, $^2H_{11/2}$, generating green $^4S_{3/2}$, $^2H_{11/2}$ − $^4I_{15/2}$ transitions. The populating pathway of the red $^4F_{9/2}$ level is as follows: after populating the $^4I_{11/2}$ level, the electrons further relax to $^4I_{13/2}$, then it is excited into $^4F_{9/2}$, generating $^4F_{9/2}$ − $^4I_{15/2}$ transitions. Besides, the nonradiative relaxation from the green $^4S_{3/2}$, $^2H_{11/2}$ level to $^4F_{9/2}$ and the cross-relaxation of $^4F_{7/2}$+$^4I_{11/2}$−$^4F_{9/2}$+$^4F_{9/2}$ is another pathway for the population of the red level.

It is known that t-$LaVO_4$ is a metastable zircon structure. To illustrate the stability of the prepared t-$LaVO_4$, the thermal properties of as-prepared samples were investigated by TG-DTA, which is exhibited in Figure 14. The first weight loss at

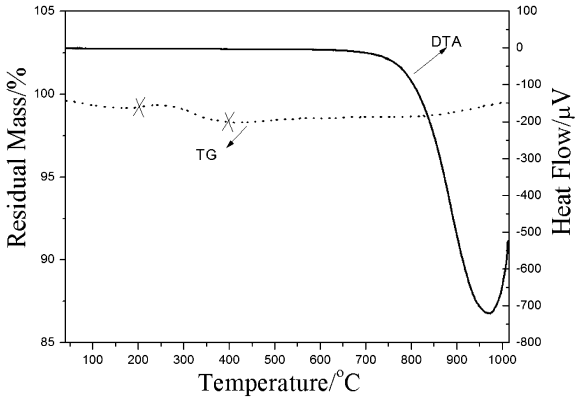

Figure 14. TG−DTA curves of t-$LaVO_4$:10%Yb^{3+}, 1%Er^{3+}.

around 40−200 °C is attributed to the evaporation of water molecules present in the sample. The second weight loss from 200 to 400 °C is because of the burnout of the remaining Na_2EDTA, which has been confirmed by FT-IR. Especially, an exothermic peak at 970 °C in the DTA curve is assigned to the phase change from zircon phase to monazite phase. Considering the strong green emission by upconversion process which can convert the NIR light to high energy photons that can be absorbed by the conventional sensitizer, such as N719 dye ((2,2 ′-bipyridyl-4,4 ′-dicarboxylic acid) ruthenium(II) complexes),[52] and therefore, it may have

DOI: 10.1021/acs.inorgchem.5b00851
Inorg. Chem. 2015, 54, 7325−7334

potential to reabsorb the emitted light by $LaVO_4$:Yb^{3+}, Er^{3+} and regenerate excitons and enhance the photovoltaic conversion of dye solar cells. Furthermore, the properties of the different fluorescence intensity ratios of the main emission lines as well as the distinguished fluorescence intensity for the two phases of $LaVO_4$, and the temperature of phase change around 970 °C supplies the possible application for temperature measurements around 970 °C.

4. CONCLUSIONS

In summary, we successfully synthesized Er^{3+}-, Er^{3+}/Yb^{3+}-doped t-$LaVO_4$ with sheaf-like morphology using the Na_2EDTA-assisted hydrothermal method. On the crystal growth process, Na_2EDTA plays an important role in the crystal splitting of the sheaf-like t-$LaVO_4$. From a comparative study on the t-$LaVO_4$:Er^{3+} and m-$LaVO_4$:Er^{3+}, it is found that Er^{3+}-doped t-$LaVO_4$ exhibited a much more brighter green emission than Er^{3+}-doped m-$LaVO_4$ using a continuous 980 nm laser diode as the excitation source. This remarkable improvement was attributed to the local structure of Er^{3+}. The study of the upconversion properties for Er^{3+}-, Er^{3+}/Yb^{3+}-doped t- and m-$LaVO_4$ indicated that two-photon processes are responsible for the green emissions via the analysis of the spectra and pump power dependence. In addition, the Er^{3+}-, Er^{3+}/Yb^{3+}-doped metastable t-$LaVO_4$ microcrystals exhibit a stable characteristic below 700 °C which was verified by TG-DTA. These properties suggest that it may be a candidate for applications such as energy relay solar cell light harvesting in the near-infrared region and optical thermometers. We believe that this study will provide new insights into the design of new upconversion materials with high efficiency.

AUTHOR INFORMATION

Corresponding Authors

*E-mail: zhangfeng.home@163.com. Fax: +86-378-3880659. Tel: +86-378-3881940.

*E-mail: ylyan@henu.edu.cn.

Notes

The authors declare no competing financial interest.

ACKNOWLEDGMENTS

This work was supported by the National Natural Science Foundation of China (Grant No. 51402088), the Postdoctoral Science Foundation of China (2013M531671), the Science and Technology Research Foundation awarded by Educational Commission of Henan Province of China (Grant no.13A430096), and the Fundamental Research Fund of provincial universities for young scientific talents (0000A40545).

REFERENCES

(1) Wang, J.; Song, H.; Xu, W.; Dong, B.; Xu, S.; Chen, B.; Yu, W.; Zhang, S. *Nanoscale* **2013**, *5*, 3412−3420.

(2) Xie, X.; Gao, N.; Deng, R.; Sun, Q.; Xu, Q.-H.; Liu, X. *J. Am. Chem. Soc.* **2013**, *135*, 12608−12611.

(3) Wang, F.; Liu, X. *Chem. Soc. Rev.* **2009**, *38*, 976−989.

(4) Cheng, Q.; Sui, J.; Cai, W. *Nanoscale* **2012**, *4*, 779−784.

(5) Calderón-Villajos, R.; Zaldo, C.; Cascales, C. *Nanotechnology* **2012**, *23*, 505205.

(6) Xu, W.; Chen, B.; Yu, W.; Zhu, Y.; Liu, T.; Xu, S.; Min, X.; Bai, X.; Song, H. *Dalton Trans.* **2012**, *41*, 13525.

(7) Sun, L.; Zhao, X.; Li, Y.; Li, P.; Sun, H.; Cheng, X.; Fan, W. *J. Appl. Phys.* **2010**, *108*, 093519.

(8) Shao, B.; Zhao, Q.; Guo, N.; Jia, Y.; Lv, W.; Jiao, M.; Lü, W.; You, H. *CrystEngComm* **2014**, *16*, 152−158.

(9) Zahedifar, M.; Chamanzadeha, Z. *JNS* **2012**, *2*, 131−137.

(10) Zhao, J.; Ma, J.; Dai, C.; Liu, Y.; Song, Z.; Sun, Y.; Fang, J.; Gao, C.; Liu, Z.; Sun, X. *J. Alloys Compd.* **2010**, *507*, L35−L37.

(11) Schwarz, H. Z. *Z. Anorg. Allg. Chem.* **1963**, *323*, 44−56.

(12) Fan, W.; Song, X.; Bu, Y.; Sun, S.; Zhao, X. *J. Phys. Chem. B* **2006**, *110*, 23247−23254.

(13) Yang, J.; Zhang, C.; Li, C.; Yu, Y.; Lin, J. *Inorg. Chem.* **2008**, *47*, 7262−7270.

(14) Ropp, R. C.; Carroll, B. *J. Inorg. Nucl. Chem.* **1973**, *35*, 1153−1157.

(15) Oka, Y.; Yao, T.; Yamamoto, N. *J. Solid State Chem.* **2000**, *152*, 486−491.

(16) Jia, C.-J.; Sun, L.-D.; You, L.-P.; Jiang, X.-C.; Luo, F.; Pang, Y.-C.; Yan, C.-H. *J. Phys. Chem. B* **2005**, *109*, 3284−3290.

(17) Jia, C.-J.; Sun, L.-D.; Luo, F.; Jiang, X.-C.; Wei, L.-H.; Yan, C.-H. *Appl. Phys. Lett.* **2004**, *84*, 5305−5307.

(18) Ma, J.; Wu, Q.; Ding, Y. *J. Nanopart. Res.* **2008**, *10*, 775−786.

(19) Wang, N.; Chen, W.; Zhang, Q.; Dai, Y. *Mater. Lett.* **2008**, *62*, 109−112.

(20) Zhang, J.; Shi, J.; Tan, J.; Wang, X.; Gong, M. *CrystEngComm* **2010**, *12*, 1079−1085.

(21) Qu, X.; Song, H.; Bai, X.; Pan, G.; Dong, B.; Zhao, H.; Wang, F.; Qin, R. *Inorg. Chem.* **2008**, *47*, 9654−9659.

(22) Chen, Z.; Chen, T.; Gong, W.; Xu, W.; Wang, D.; Wang, Q. *J. Am. Ceram. Soc.* **2013**, *96*, 1857−1862.

(23) Wang, F.; Song, F.; Zhang, G.; Han, Y.; Li, Q.; Ming, C.; Tian, J. *J. Appl. Phys.* **2014**, *115*, 134310.

(24) Cheng, F.; Xia, Z.; Jing, X.; Wang, Z. *Phys. Chem. Chem. Phys.* **2015**, *17*, 3689−3696.

(25) Yu, S.; Zhi, Y.; Su, H. *J. Nanosci. Nanotechnol.* **2014**, *14*, 3380−3386.

(26) Zahedifar, M.; Chamanzadeh, Z.; Hosseinpoor Mashkani, S. M. *J. Lumin.* **2013**, *135*, 66−73.

(27) He, F.; Yang, P.; Wang, D.; Niu, N.; Gai, S.; Li, X.; Zhang, M. *Dalton T.* **2011**, *40*, 11023−11030.

(28) Jia, C. J.; Sun, L. D.; Yan, Z. G.; Pang, Y. C.; Lü, S. Z.; Yan, C. H. *Eur. J. Inorg. Chem.* **2010**, *2010*, 2626−2635.

(29) Heer, S.; Kömpe, K.; Güdel, H.-U.; Haase, M. *Adv. Mater.* **2004**, *16*, 2102−2105.

(30) Rice, C. E.; Robinson, W. R. *Acta Crystallogr., Sect. B: Struct. Crystallogr. Cryst. Chem.* **1976**, *B32*, 2232−2233.

(31) Kresse, G.; Hafner, J. *Phys. Rev. B: Condens. Matter Mater. Phys.* **1993**, *47*, 558.

(32) Perdew, J. P.; Burke, K.; Ernzerhof, M. *Phys. Rev. Lett.* **1996**, *77*, 3865.

(33) Singh, D. *Planewaves, Pseudopotentials, and the LAPW Method*; Kluwer Academic Publishers: Boston, 1994.

(34) Blaha, P. Schwarz, K.; Madsen, G. K. H.; Kvasnicka, D.; Luitz, J. *WIEN2k: An Augmented Plane Wave + Local Orbitals Program for Calculating Crystal Properties*; Vienna University of Technology: Vienna, Austria, 2001.

(35) Engel, E.; Vosko, S. H. *Phys. Rev. B: Condens. Matter Mater. Phys.* **1993**, *47*, 13164.

(36) Dai, Q.; Song, H.; Ren, X.; Lu, S.; Pan, G.; Bai, X.; Dong, B.; Qin, R.; Qu, X.; Zhang, H. *J. Phys. Chem. C* **2008**, *112*, 19694−19698.

(37) Xie, B.; Lu, G.; Wang, Y.; Guo, Y.; Guo, Y. *J. Alloys Compd.* **2012**, *544*, 173−180.

(38) Sun, Y. J.; Liu, H. J.; Wang, X.; Kong, X. G.; Zhang, H. *Chem. Mater.* **2006**, *18*, 2726−2733.

(39) Weng, X.; Yang, Q.; Wang, L.; Xu, L.; Sun, X.; Liu, J. *CrystEngComm* **2013**, *15*, 10230−10237.

(40) Thirumalai, J.; Chandramohan, R.; Vijayan, T. A. *Mater. Chem. Phys.* **2011**, *127*, 259−264.

(41) Luo, F.; Jia, C. J.; Song, W.; You, L. P.; Yan, C. H. *Cryst. Growth Des.* **2005**, *5*, 137−142.

(42) Sheng, Y. Q.; Liu, J.; Xu, L. L.; Zhai, D.; Zhang, Z. G.; Cao, W. W. *Solid State Commun.* **2010**, *150*, 1048−1051.

DOI: 10.1021/acs.inorgchem.5b00851
Inorg. Chem. 2015, 54, 7325−7334

(43) Sun, L.; Zhao, X.; Li, Y.; Li, P.; Sun, H.; Cheng, X.; Fan, W. *J. Appl. Phys.* **2010**, *108*, 093519.
(44) He, Y.; Cai, J.; Zhang, L.; Wang, X.; Lin, H.; Teng, B.; Zhao, L.; Weng, W.; Wan, H.; Fan, M. *Ind. Eng. Chem. Res.* **2014**, *53*, 5905−5915.
(45) Parhi, P.; Manivannan, V. *Solid State Sci.* **2008**, *10*, 1012−1019.
(46) Pollnau, M.; Gamelin, D. R.; Lüthi, S. R.; Güdel, H. U.; Hehlen, M. P. *Phys. Rev. B: Condens. Matter Mater. Phys.* **2000**, *61*, 3337.
(47) Etchart, I.; Huignard, A.; Bérard, M.; Nordin, M. N.; Hernández, I.; Curry, R. J.; Gillin, W. P.; Cheetham, A. K. *J. Mater. Chem.* **2010**, *20*, 3989−3994.
(48) Mahalingam, V.; Hazra, C.; Naccache, R.; Vetrone, F.; Capobianco, J. A. *J. Mater. Chem. C* **2013**, *1*, 6536−6540.
(49) Yu, W.; Xu, W.; Song, H.; Zhang, S. *Dalton Trans.* **2014**, *43*, 6139−6147.
(50) Zhang, D. L.; Wu, C.; Yang, Q. Z.; Sun, L.; Xu, Y. H.; Pun, E. Y. B. *Appl. Phys. B: Lasers Opt.* **2009**, *95*, 335−340.
(51) Wang, Y.; Xu, W.; Zhu, Y.; Xu, S.; Cui, H.; Song, H. *J. Mater. Chem. C* **2014**, *2*, 4642−4650.
(52) Shan, G. B.; Demopoulos, G. P. *Adv. Mater.* **2010**, *22*, 4373−4377.

DOI: 10.1021/acs.inorgchem.5b00851
Inorg. Chem. 2015, 54, 7325−7334